Rare Met. (2025) 44(6):3909–3919
https://doi.org/10.1007/s12598-025-03245-7

RARE METALS

ORIGINAL ARTICLE

Capacitance decay mechanism of vanadium nitride supercapacitor electrodes in KOH electrolytes

Xiu-Li Li, Hao Song, Yong-Hui Zhang, Yu-Lei Ren, Qi-Fei Guo, Zi-Huan Tang, Zhuo Li*, Biao Gao*, Paul K. Chu, Kai-Fu Huo*

Received: 21 November 2024 / Revised: 31 December 2024 / Accepted: 1 January 2025 / Published online: 4 March 2025

Abstract Vanadium nitride (VN) is a promising pseudocapacitive material due to the high theoretical capacity, rapid redox Faradaic kinetics, and appropriate potential window. Although VN shows large pseudocapacitance in alkaline electrolytes, the electrochemical instability and capacity degradation of VN electrode materials present significant challenges for practical applications. Herein, the capacitance decay mechanism of VN is investigated and a simple strategy to improve cycling stability of VN supercapacitor electrodes is proposed by introducing VO_4^{3-} anion in KOH electrolytes. Our results show that the VN electrode is electrochemical stabilization between −1.0 and −0.4 V (vs. Hg/HgO reference electrode) in 1.0 M KOH electrolyte, but demonstrates irreversible oxidation and fast capacitance decay in the potential range of −0.4 to 0 V. In situ electrochemical measurements reveal that the capacitance decay of VN from −0.4 to 0 V is ascribed to the irreversible oxidation of vanadium (V) of N–V–O species by oxygen (O) of OH^-. The as-generated oxidization species are subsequently dissolved into KOH electrolytes, thereby undermining the electrochemical stability of VN. However, this irreversible oxidation process could be hindered by introducing VO_4^{3-} in KOH electrolytes. A high volumetric specific capacitance of 671.9 $F{\cdot}cm^{-3}$ (1 $A{\cdot}cm^{-3}$) and excellent cycling stability (120.3% over 1000 cycles) are achieved for VN nanorod electrode in KOH electrolytes containing VO_4^{3-}. This study not only elucidates the failure mechanism of VN supercapacitor electrodes in alkaline electrolytes, but also provides new insights into enhancing pseudocapacitive energy storage of VN-based electrode materials.

Keywords Vanadium nitride; Capacitance decay; Pseudocapacitance; Oxidation mechanism; Supercapacitors

Xiu-Li Li and Hao Song have contributed equally to this work.

Supplementary Information The online version contains supplementary material available at https://doi.org/10.1007/s12598-025-03245-7.

X.-L. Li, H. Song, Y.-H. Zhang, Y.-L. Ren, Q.-F. Guo, Z.-H. Tang, Z. Li*, B. Gao*
The State Key Laboratory of Refractories and Metallurgy and Institute of Advanced Materials and Nanotechnology, Wuhan University of Science and Technology, Wuhan 430081, China
e-mail: zhuo_li@wust.edu.cn

B. Gao
e-mail: gaobiao@wust.edu.cn

P. K. Chu
Department of Physics and Department of Materials Science and Engineering, City University of Hong Kong, Hong Kong 999077, China

K.-F. Huo*
Wuhan National Laboratory for Optoelectronics (WNLO), Huazhong University of Science and Technology, Wuhan 430074, China
e-mail: kfhuo@hust.edu.cn

1 Introduction

Electrochemical supercapacitors (SCs) are promising charge storage devices that can offer high power densities, long cycling life, and excellent reversibility compared to batteries [1–3]. Therefore, there is increasing interest in various fields, including hybrid or electric vehicles, electronic devices, aircraft, and smart grids [4–8]. The electrochemical properties of SCs are primarily determined by the electrode materials. Carbon-based electrode materials are widely investigated for SCs due to their high conductivity, large

surface areas, and excellent electrochemical stability; however, the carbon electrodes that store energy via ions adsorption/desorption generally exhibit low specific capacitance (90−250 $F{\cdot}g^{-1}$) [9, 10]. Pseudocapacitive materials that store charges by rapid surface redox reactions have larger capacitance compared with porous carbon materials, thereby enabling high energy densities [11–14]. Vanadium nitride (VN) is a promising pseudocapacitive material, which has high specific capacity (1340 $F{\cdot}g^{-1}$, 2 $mV{\cdot}s^{-1}$) and electrical conductivity (1.67 × 10^6 $\Omega^{-1}{\cdot}m^{-1}$) [15–18]. Previous reports indicate that VN electrodes have larger capacitance in alkaline electrolytes compared with acidic and neutral electrolytes [19–21]. However, VN electrode materials exhibit poor electrochemical stability and fast capacitance degradation in alkaline electrolytes, which present significant challenges for practical applications in aqueous supercapacitors.

Current research activities predominantly focus on enhancing the stability of VN in KOH electrolytes by carbon coating or electrolyte additives. For example, Liu et al. embedded VN into an N-doped graphene framework to prevent the direct interactions of VN with the electrolyte, resulting in high capacity retention of 94.8% after 2000 cycles in 2.0 M KOH [22]. Haye et al. have used a V^{5+}-containing KOH electrolytes to form a stable oxide/oxynitride layer on the surface of VN, thereby reducing the capacitance loss from 59% to 23% [23]. Despite recent progress, the inherent degradation mechanisms of VN electrodes are not clear, and some results are even contradictory. For instance, some reports suggest that the surface redox reaction of VN in KOH proceeds by $V^{3+}N_xO_y + 2OH^- \rightarrow V^{3+}N_xO_y//OH^- + V^{2+}N_xO_y - OH$ [18, 24]. However, Djire et al. have proposed an alternative balanced redox reaction for VN in aqueous alkaline media of $V^{3+}N + 2OH^- + e^- \rightarrow V^{2+}N(OH^-)_2$ [25].

In this study, the capacitance decay mechanism of VN in KOH is studied by in situ attenuated total reflectance–Fourier transform infrared spectroscopy (ATR–FTIR) and electrochemical quartz crystal microbalance (EQCM). Our results reveal that VN is stable between −1.0 and −0.4 V (vs. Hg/HgO reference electrode); however, its capacitance decreases sharply in the voltage range of −0.4 to 0 V due to the irreversible oxidation. The irreversible oxidation process of VN involves the oxidation of N–V–O and V–N by OH^- and dissolved oxygen, followed by the dissolution of vanadium oxide species into the electrolyte. This irreversible oxidation results in the fast capacitance decay of VN electrode in KOH electrolytes between −0.4 and 0 V. However, the electrochemical oxidation and dissolution could be hampered by adding a redox-active additive (VO_4^{3-}) into the KOH electrolyte, enabling much improved cycling stability. And the symmetrical all-solid-state flexible SC composed of VN electrode and KOH-VO_4^{3-}/PVA gel electrolyte shows a high energy density of 40.8 $mWh{\cdot}cm^{-3}$ (69.4 $Wh{\cdot}kg^{-1}$) at 496.7 $mW{\cdot}cm^{-3}$ (843.9 $W{\cdot}kg^{-1}$), suggesting large potential in next-generation electrochemical energy storage devices.

2 Experimental

2.1 Fabrication of VN nanorods

NH_4VO_3 (1.17 g) and 1 mL of CH_3COOH were mixed in 10 mL of deionized water until NH_4VO_3 dissolved completely. The solution was transferred to a 50 mL autoclave and underwent a hydrothermal treatment at 180 °C for 24 h. After cooling to room temperature naturally, the yellow precipitate of lamellar $NH_4V_3O_8$ was filtered, washed with distilled water, and vacuum freeze-dried for 12 h. The VN nanorods were produced by annealing the lamellar $NH_4V_3O_8$ at 550 °C for 2 h under NH_3.

2.2 Material characterization

The morphology and microstructure of VN nanorods were examined using field emission scanning electron microscopy (SEM, JSM-6700F) and transmission electron microscopy (TEM, JEM-F200). The crystalline structure was determined by X-ray diffraction (XRD, SmartLab) using a Cu Kα source. The surface chemistry compositions were analyzed by X-ray photoelectron spectroscopy (XPS, AXIS SUPRA +).

2.3 Electrochemical measurements

The electrochemical measurements were taken on the PARSTAT MC-200 electrochemical workstation with a three-electrode configure in the KOH electrolyte without and with the addition of VO_4^{3-} with Pt sheet as the counter electrode, and Hg/HgO (1.0 M KOH) as the reference electrode. The synthesis route involves adding 0.1 M V_2O_5 to 1.6 M KOH ($V_2O_5 + 6KOH \rightarrow 2K_3VO_4 + 3H_2O$) solution to prepare the 1.0 M KOH electrolyte containing 0.2 M VO_4^{3-}. Additionally, the 1.0 M KOH electrolyte containing 0.1 and 0.5 M VO_4^{3-} was prepared by a similar route. The VN, acetylene black, and polytetrafluoroethylenes (PTFE) are mixed in deionized water with a mass ratio of 8:1:1 to yield a slurry, which was spread on carbon paper with an area of about 1 cm^2. The working electrode was vacuum-dried at 80 °C for 24 h. Electrochemical impedance spectroscopy (EIS) was performed between 0.01 and 100 kHz with an amplitude potential of 5 mV. The volumetric specific capacitances C_v ($F{\cdot}cm^{-3}$) were calculated according to Eq. (1):

$$C_V = \frac{(I \times \Delta t)}{(\Delta V \times V)} \quad (1)$$

where I (A) represents the response current, Δt (s) designates the discharge time, ΔV (V) refers to the voltage window, and V (cm^3) denotes the volume of the electrode.

The all-solid-state symmetrical device was fabricated by divided two similar VN electrodes by KOH-VO_4^{3-}/PVA gel electrolyte. The KOH-VO_4^{3-}/PVA gel electrolyte was prepared by dissolving 1.792 g of KOH, 0.364 g of V_2O_5, and 2.000 g of PVA into 20 mL of deionized water. The mixture was then heated to 85 °C for 3 h under vigorous stirring. The total volumetric specific capacitance (C_{cell}, $F{\cdot}cm^{-3}$), volumetric energy density (E, $Wh{\cdot}cm^{-3}$), and power density (P, $W{\cdot}cm^{-3}$) were obtained by Eqs. (2–4):

$$C_{Cell} = \frac{(I \times \Delta t)}{(\Delta V \times V)} \quad (2)$$

$$E = \frac{(0.5 C_{Cell} \times \Delta V^2)}{3600} \quad (3)$$

$$P = \frac{(E \times 3600)}{\Delta t} \quad (4)$$

where V (cm^3) is the total volume of both positive and negative electrodes, ΔV (V) is the potential range, and Δt (s) is the discharge time.

2.4 EQCM measurement

The mass changes of the electrode were tracked by electrochemical quartz crystal microbalance (EQCM, QCM922). The electrochemical measurements were taken in parallel with EQCM on the PARSTAT MC-200 electrochemical workstation. The frequency data were collected accompanied with cyclic voltammetry (CV) at 20 $mV{\cdot}s^{-1}$. The mass change was calculated by Eq. (5) [26–28]:

$$\Delta m = -\frac{(\Delta f \times A \times \sqrt{\mu\rho})}{2f_0^2} \quad (5)$$

where Δf represents the change in the resonant frequencies of the gold-coated quartz crystal electrode, A denotes the active crystal surface (0.198 cm^2), μ refers to the shear modulus of quartz (2.947×10^{11} $g{\cdot}cm^{-1}{\cdot}s^{-2}$), ρ represents the density of quartz (2.650 $g{\cdot}cm^{-3}$), and f_0 is the reference frequency of the quartz crystal (9.000 MHz). According to this equation, the change of 1 Hz is equal to 1.068 ng.

2.5 In situ ATR–FTIR

Attenuated total reflectance–Fourier transform infrared spectroscopy (ATR–FTIR) was conducted on the Nicolet iS50 (Thermo-Fisher Scientific) equipped with an extended range diamond ATR accessory (Shanghai Linglu Instrument Co. Ltd). FTIR spectra were acquired every 100 s, while CV was performed at a scanning rate of 1 $mV{\cdot}s^{-1}$. The FTIR spectra were acquired using a liquid nitrogen-cooled HgCrTe (MCT/A) detector with a resolution of 4 cm^{-1} in the range of 650–4000 cm^{-1}, and 32 scans were taken for each spectrum.

3 Results and discussion

Figure 1a schematically depicts the synthesis procedure of VN nanorods. The SEM image in Fig. 1b reveals that the $NH_4V_3O_8$ precursor has a uniform and smooth surface, and the X-ray diffraction (XRD) pattern can be indexed to the monoclinic phase of $NH_4V_3O_8$ (JCPDS card No. 88–1473) (Fig. 1c). After nitridation, the XRD pattern is ascribed to cubic VN (JCPDS card No. 35–0768) and the peaks corresponding to $NH_4V_3O_8$ disappear (Fig. 1c). The SEM image reveals that the VN has a rodlike morphology with a width of 900 nm and a length of 2.1 μm (Fig. 1d). The TEM images of VN nanorods in Fig. 1e, f reveal lattice fringes of 0.205 nm matching the (200) crystal planes of VN [29]. The XPS spectra of VN nanorods exhibit three sub-peaks corresponding to V–N (513.9 and 521.2 eV), N–V–O (515.4 and 522.7 eV), and V–O (517.1 and 524.5 eV) (Fig. 1g) [30, 31], confirming the synthesis of VN nanorods.

Figure 2 depicts the capacitance retention and morphology evolution of VN in 1.0 M KOH electrolyte during cycling, which are operated in three potential windows of −1.0 to 0 V, −1.0 to −0.4 V, and −0.4 to 0 V at a current density of 1 $A{\cdot}cm^{-3}$. The corresponding galvanostatic charging/discharging (GCD) plots before and after cycling are shown in Fig. S1. VN electrode exhibits remarkable stability manifested by a capacitance retention of almost 100% between −1.0 and −0.4 V (Fig. 2a); however, the capacitance retention of VN drops to 35.5% and 28.3% after 1000 cycling in the potential ranges of −1.0 to 0 V and −0.4 to 0 V. These results reveal that the capacitance decay and electrochemical degradation of VN in KOH mainly occur in the potential range between −0.4 and 0 V. The surface chemical states of the VN electrode after 1000 cycling are determined by XPS (Fig. S2). The V 2p spectra (Fig. 2b) reveal three peaks corresponding to V–N, N–V–O, and V–O in the potential range of −1.0 to −0.4 V, which are similar to the pristine VN nanorods. However, the V–N and N–V–O peaks are nearly undetectable in the potential windows of −1.0 to 0 V and −0.4 to 0 V and only the V–O peak is observed, indicating the irreversible conversion of VN into vanadium oxide species. N 1s spectra shown in Fig. 2c demonstrate that the N signal of V–N is inherited in the potential range

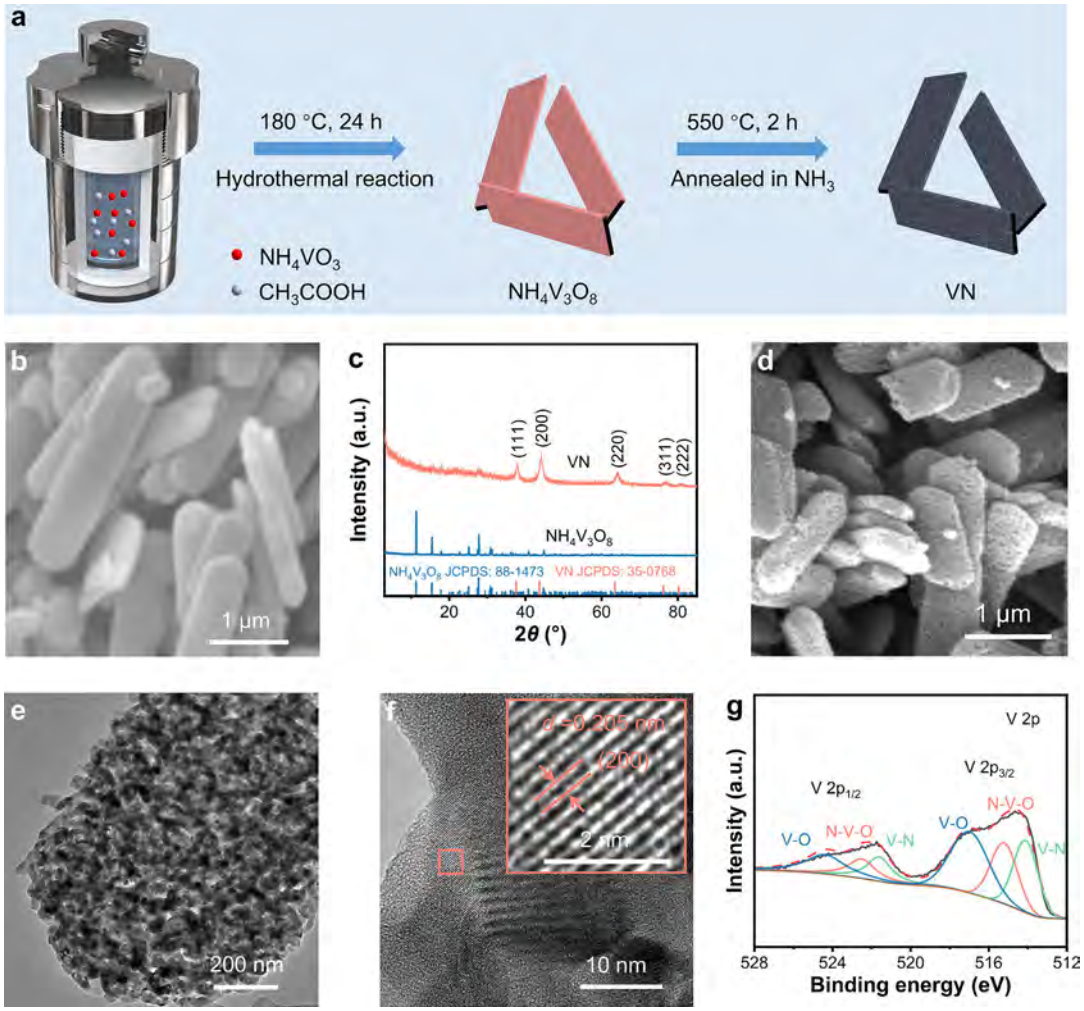

Fig. 1 Preparation and characterization of VN nanorods. **a** Synthesis scheme of VN nanorods; **b** SEM image of $NH_4V_3O_8$; **c** XRD patterns of $NH_4V_3O_8$ and VN nanorods; **d** SEM image, **e, f** TEM images, and **g** V 2p spectrum of VN nanorods

between −1.0 and −0.4 V after 1000 cycles; however, the peak of N 1s is disappeared in the potential windows of −1.0 to 0 V and −0.4 to 0 V, further confirming that oxidation of VN occurs in the voltage range of −0.4 to 0 V. The morphologies of VN nanorods before and after 1000 cycling are depicted in Figs. S3, 2d−f. The cycled VN electrode in the potential range of −1.0 to −0.4 V shows pristine morphology of VN nanorods. On the contrary, the rodlike morphology is corroded in the potential windows of −1.0 to 0 V and −0.4 to 0 V. Additionally, TEM images of VN electrode after cycle in the voltage range of −0.4 to 0 V reveal a notable presence of amorphous components and interlayer spacing of 0.169 and 0.204 nm, corresponding to the (220) and (022) lattice plane of cubic V_2O_5 (Fig. 2g−i), indicating severe oxidation of the VN electrode in KOH electrolytes within this voltage range. Figure S4 presents the CV curves for various cycles in the potential range of −0.4 to 0 V. The oxidation peak increases initially, but declines rapidly afterward, ultimately vanishing after 1000 cycles as a result of irreversible oxidation. These results reveal that VN is unstable within the potential range of −0.4 to 0 V, mainly originating from the irreversible electrochemical oxidation.

To elucidate the electrochemical oxidation mechanism of VN in KOH electrolytes, oxygen-free VN is prepared by thermal nitridation of VS_2 precursor. As depicted in Figs. 3a, S5, the oxygen-free VN exhibits poor stability in the KOH electrolyte with a capacity retention of only 37.6% after 1000 cycles in the potential range of −1.0 to 0 V. However, the oxygen-free VN exhibits an enhanced cyclability with 94.3% capacity retention after 1000 cycles if the dissolved oxygen in the electrolyte is removed by bubbling N_2. These results indicate that V–N bonds are readily oxidized by dissolved oxygen in the KOH electrolyte. For comparison, the oxygen-free VN electrode exhibits a capacitance retention of almost 100% in the potential range between −1.0 and −0.4 V even if the dissolved oxygen in KOH is remained (Fig. S6). This

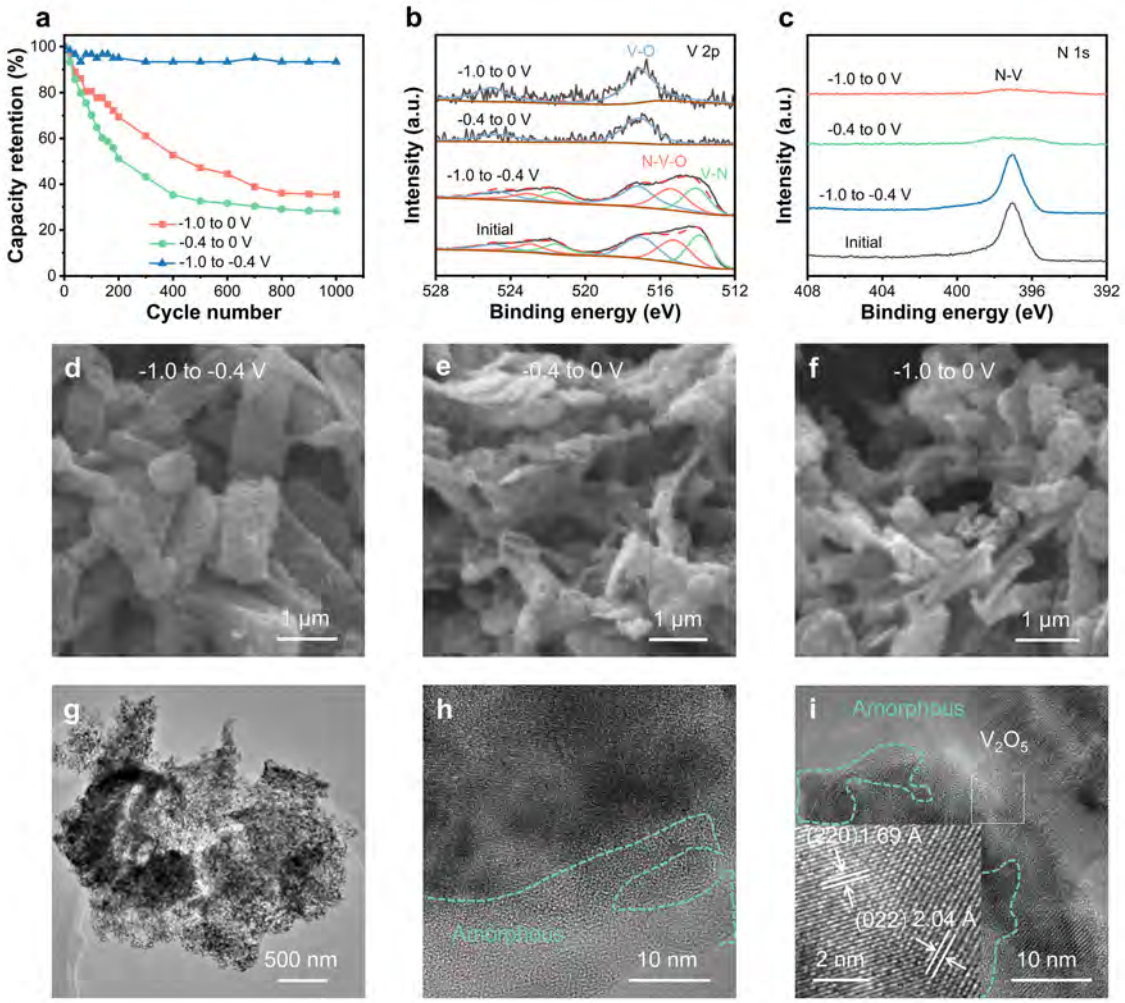

Fig. 2 Electrochemical properties and morphologies evolution of VN operated in different potential ranges (−1.0 to −0.4 V, −0.4 to 0 V, and −1.0 to 0 V). **a** Relative capacity retention curves of VN at three different potential ranges, **b** XPS V 2p spectra, **c** N 1s spectra, and **d**−**f** SEM images of VN electrode after 1000 cycles in different potential windows; **g**−**i** TEM images of VN electrode after cycle in the voltage range of −0.4 to 0 V

indicates that the oxidation reaction between V–N bonds and dissolved oxygen occurs in the voltage range of −0.4 to 0 V. On the contrary, despite continuous N_2 flow during cycling, VN nanorod electrode still exhibits a disappointing capacity retention rate of 50.5% after 1000 cycles in the voltage range between −1.0 and 0 V. After excluding the oxidation of V–N caused by dissolved oxygen, the remaining capacity decline of VN in the KOH electrolyte attributed to the oxidation of N–V–O species. Thus, the co-oxidation of V–N and N–V–O in the voltage range between −0.4 and 0 V results in the poor cyclic stability of VN in the KOH electrolyte.

To study the interactions between OH^- and N–V–O species, in situ FTIR is carried out by bubbling N_2 in 1.0 M KOH (Fig. S7). Figure 3b displays the potential-dependent in situ FTIR spectra. The absorption peak at ∼ 852 cm^{-1} corresponds to the stretching vibration mode of V–O. During charging from −1.0 to 0 V, the strength of characteristic V–O band increases gradually. When the discharge voltage returns to −1.0 V, the peak intensity of the V–O bond diminishes, but remains higher than the initial peak intensity. The dissymmetry periodic intensity change of V–O is also evident in the mapping mode of the IR signal evolution for the charging–discharging process, as shown in Fig. 3c. These results indicate that the electrochemical oxidation of N–V–O in KOH involves the active vanadium sites in N–V–O interacting with OH^- to form vanadium oxide. Subsequently, we perform ex situ XPS analysis of the VN electrode at various charge states to accurately elucidate the oxidation processes. As the advancement of the charging state, as illustrated in Figs. 3d, S8 and Table S1, the V–O peak intensities slightly increase while those of V–N peak decrease. Concurrently, the V–O/V–N ratio increases from 1.20 to 1.87, suggesting

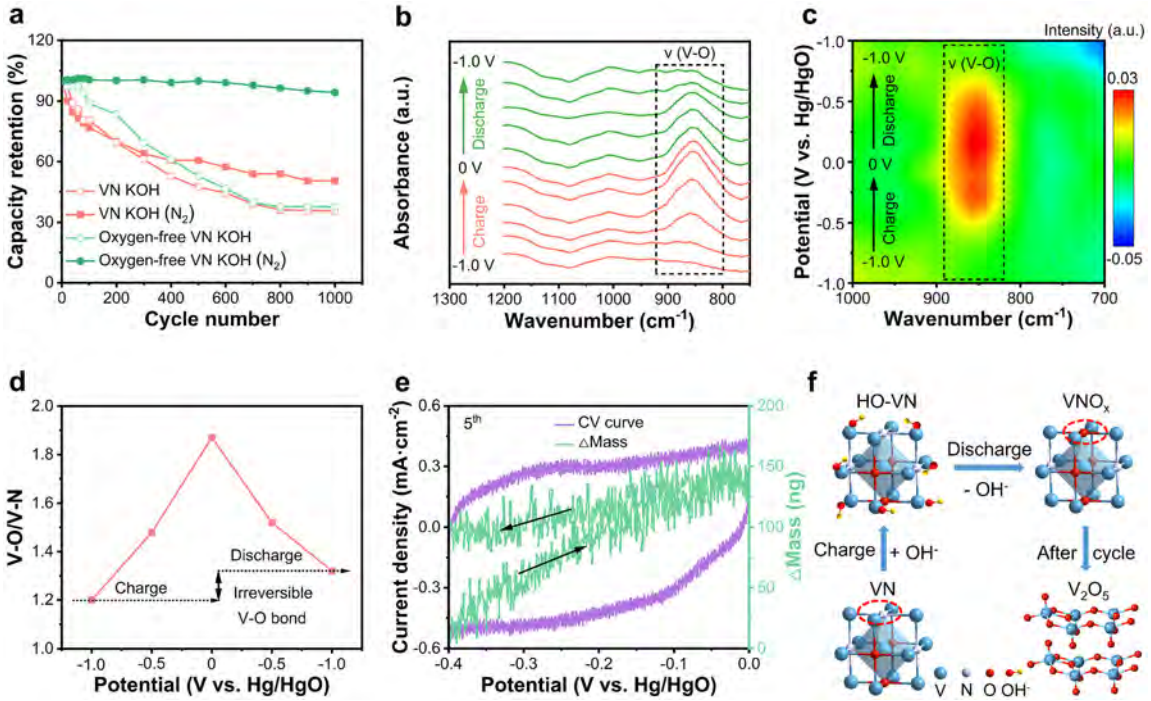

Fig. 3 Electrochemical characterizations of the oxidation of VN in KOH. **a** Cyclic performances of VN and oxygen-free VN with and without bubbling N_2 in 1.0 M KOH in the potential range of −1.0 to 0 V; **b, c** in situ IR spectra of the VN in 1.0 M KOH during charge and discharge; **d** ratios of V–O to V–N of the VN electrode derived from the V 2p spectra for different charge states; **e** 5th cycle CV curve (20 $mV \cdot s^{-1}$) and mass change of the VN-coated quartz electrode between −0.4 and 0 V; **f** oxidation schematic diagram of VN in KOH electrolytes

that the oxidation reaction is predominant in this process. Upon discharging, the V–O/V–N ratio partially recovers to 1.32, demonstrating an irreversible change/charging process within the −1.0 to 0 V voltage range. To further investigate the irreversible oxidation of VN in KOH electrolytes in the potential range between −0.4 and 0 V, the variation in the mass (Δm) of the VN electrode is determined by EQCM (Fig. S9). Figure 3e shows the CV curve (purple line) together with the corresponding mass change curve (green line) of VN. The electrode mass increases during anodic scanning (charging) and decreases during cathodic scanning (discharging). However, the VN electrode exhibits a mass change of 151.3 ng during the charging process and a decrease of only 60.9 ng during the discharging process, indicating irreversible mass changes. This result further suggests that the formation of irreversible V–O bonds is a critical factor contributing to the instability of VN electrode in the potential range between −0.4 and 0 V (Fig. 3f).

The mass variation (Δm) of the VN electrode during the cycle in different potential ranges is depicted in Figs. 4a, S10, S11. In the potential range of −1.0 to −0.4 V, Δm decreases slightly from 0.372 in the first cycle to 0.346 μg after the 600th cycle, demonstrating the excellent stability of the VN electrode. In contrast, the VN electrode experiences significant mass loss in the potential ranges of −0.4 to 0 V and −1.0 to 0 V, with Δm reducing from 0.058 to 0.004 μg and 0.408 to 0.034 μg, respectively. This decrease suggests that the number of active ions participating in the electrochemical reaction diminishes, leading to a gradual loss of mass from the VN electrode material in the potential range of −0.4 to 0 V. Then, the dissolution of the oxidization species of VN into KOH is monitored by UV–Vis spectrophotometry. Figure 4b shows a distinct VO_4^{3-} absorption peak at 271 nm, confirming the formation of VO_4^{3-} during cycling in the potential windows of −1.0 to 0 V and −0.4 to 0 V. When the cycling potential range is adjusted to −1.0 to −0.4 V, there is a notable reduction in the intensity of the VO_4^{3-} absorption peak, and the weak peak is attributed to the dissolution of inherent surface oxides. In brief, the poor stability of VN in KOH arises from the irreversible oxidation of V–N and N–V–O and the dissolution of oxidation products in the potential range between −0.4 and 0 V, resulting in fast pseudocapacitance decay and unsatisfactory cycling stability in KOH electrolytes (Fig. 4c).

After obtaining a clearer picture of the capacitance decay mechanism, we aim to develop a suitable method to improve the cyclability of VN by incorporating an additive (VO_4^{3-}) into the KOH electrolyte. The irreversible binding between OH^- and N–V–O is the primary cause of VN oxidation. To evaluate the enhancement of VN stability by

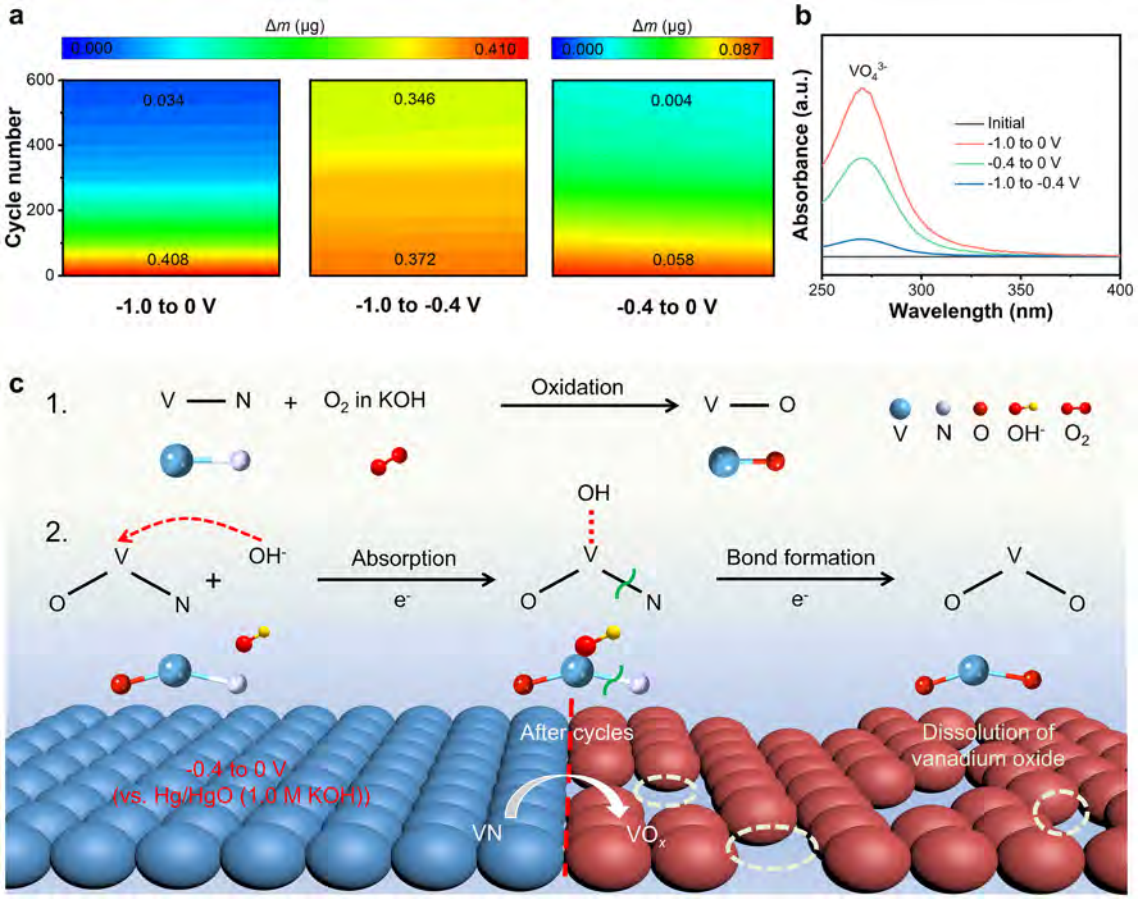

Fig. 4 Oxidation mechanism of VN in the potential range of −0.4 to 0 V. **a** Mass changes of the VN electrode during cycling; **b** UV–Vis absorption spectra of the KOH electrolyte before and after cycling in various potential windows (−1.0 to 0 V, −1.0 to −0.4 V, and −0.4 to 0 V); **c** oxidation diagram of VN in KOH electrolytes

adding VO_4^{3-} to the KOH electrolyte, we prepared the KOH-VO_4^{3-} electrolyte while maintaining a consistent OH^- concentration of 1.0 M. Typically, we prepared a 1.0 M KOH electrolyte containing 0.2 M VO_4^{3-} by dissolving 0.1 M V_2O_5 in 1.6 M KOH. The redox-active additive can improve the chemical equilibrium shift of the VN dissolution reaction to stabilize the oxide/oxynitride layer on the VN surface [23, 32]. This enhancement is confirmed by the post-cycling SEM image. As shown in Fig. S12, the VN electrode cycled in the 1.0 M KOH electrolyte with 0.2 M VO_4^{3-} inherits the initial morphology (Fig. S3). To further validate the oxidation stability, a series of electrochemical characterizations are performed. According to the linear sweep voltammetry (LSV) curves (Fig. 5a), the VN electrode in the 1.0 M KOH without the addition of VO_4^{3-} shows a sharply higher current when the voltage exceeds −0.4 V. In contrast, the oxidation potential shifts to 1.1 V after adding 0.2 M VO_4^{3-} to 1.0 M KOH. This shift enables the electrode material to undergo rapid and reversible Faradaic reactions within the voltage range of −1.0 to 0 V, thereby enhancing the redox reaction kinetics of the VN electrode. Figure 5b shows the long cycling characteristics of VN in KOH electrolytes with and without VO_4^{3-}. With VO_4^{3-} in the KOH electrolyte, the capacity retention of VN increases from 35.5% to 120.3%. The capacity retention exhibits an increasing trend in the early stages of cycling. This is attributed to the gradual infiltration of VO_4^{3-} ions, which have a larger ionic radius, into the interior of the electrode material, thereby contributing to a portion of the capacity. As a result, the specific capacity of VN initially increases and then stabilizes. Additionally, as the concentration of VO_4^{3-} increases from 0.1 to 0.2 M, the volumetric specific capacity rises from 508.6 to 671.9 $F{\cdot}cm^{-3}$ (Fig. S13). When the concentration of VO_4^{3-} further increases to 0.5 M, the volumetric specific capacity gradually decreases to 601.7 $F{\cdot}cm^{-3}$. With the addition of VO_4^{3-}, the volumetric specific capacity remains consistently higher than that observed in the absence of VO_4^{3-}. Furthermore, the volumetric specific capacitances under 0.2 M VO_4^{3-} are measured to be 671.9, 609.0, 538.1, 494.8, and 429.9 $F{\cdot}cm^{-3}$ at 1, 2, 5, 10, and 20 $A{\cdot}cm^{-3}$, respectively,

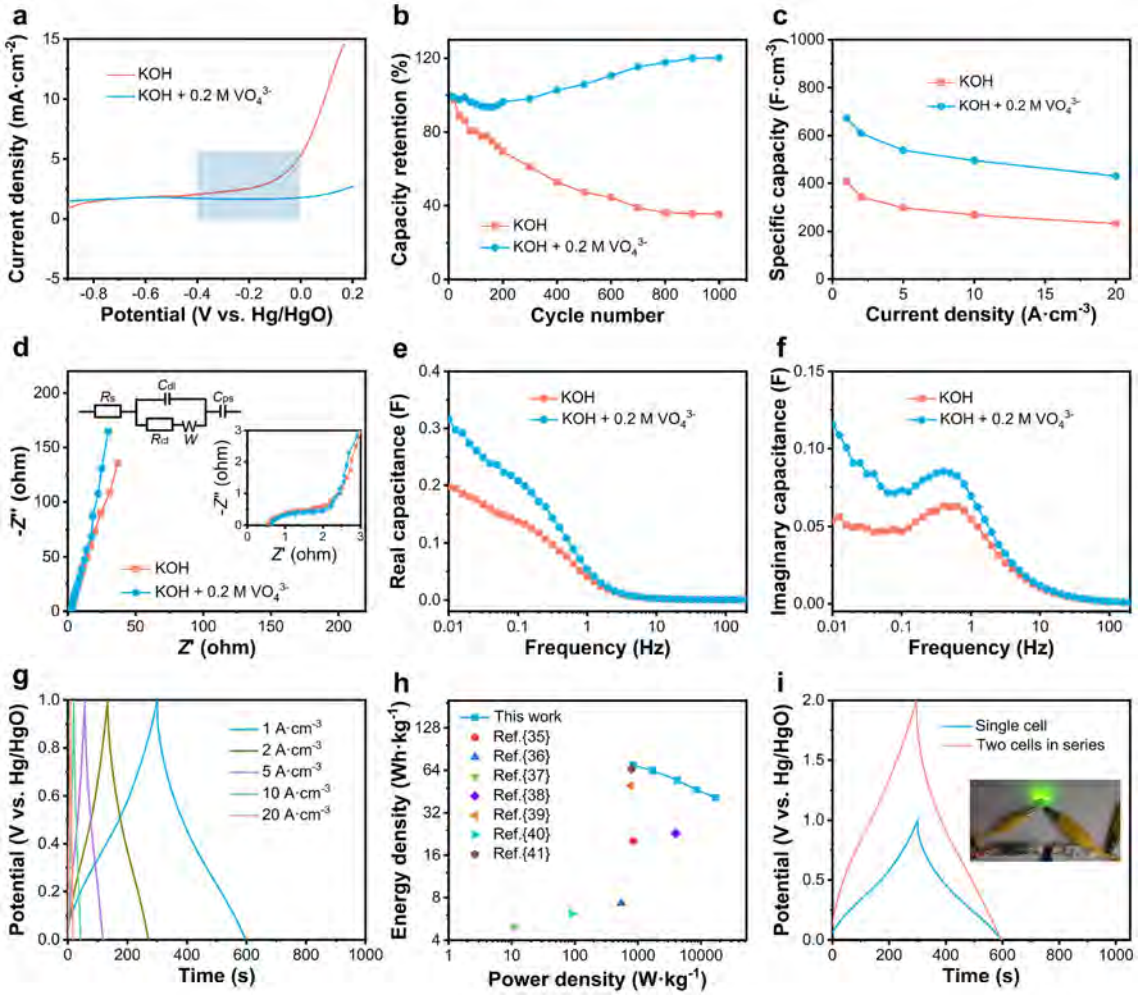

Fig. 5 Electrochemical characteristics of VN in the 1.0 M KOH electrolyte with and without the addition of 0.2 M VO_4^{3-}. **a** LSV curves, **b** relative capacity retention, **c** rate capability, **d** Nyquist plots, **e** real capacitance, and **f** imaginary capacitance as a function of frequency for the VN electrode cycling in the 1.0 M KOH electrolyte with and without VO_4^{3-}; **g** GCD curves of the VN-based device at different current densities; **h** Ragone plots of the device; **i** GCD curves of the single and two devices in series at a current density of 1 A·cm^{-3}, the inset is the digital picture of the green LED bulb (1.8 V) light by two devices in series

which is superior to that in the 1.0 M KOH electrolyte (406.4, 343.2, 296.8, 267.7, and 232.2 F·cm^{-3}) (Figs. 5c, S14). These results clearly indicate the significantly enhanced electrochemical stability and specific capacity following the addition of VO_4^{3-} to the KOH electrolyte. Figure 5d depicts the Nyquist plots of VN in KOH electrolytes with and without VO_4^{3-}. The similar EIS curves show that the incorporation of VO_4^{3-} into the KOH electrolyte does not influence charge transfer and ion diffusion during the electrochemical process. In addition, the capacitance at the low-frequency region, which is a combination of the real and imaginary parts of the capacitance, is expressed by Eq. (6) [33, 34]:

$$C(\omega) = C'(\omega) - jC''(\omega) \tag{6}$$

where C' and C'' represent the real and imaginary parts of the capacitance, respectively. Figure 5e, f illustrates the real and imaginary components of the capacitor derived from the EIS data. Notably, both the real and imaginary capacitance values exhibit a strong frequency dependence, demonstrating resistive behavior in the high-frequency region and capacitive behavior in the low-frequency region. With VO_4^{3-} present in KOH electrolytes, the real (C') and imaginary (C'') capacitance values of VN in the low-frequency region significantly enhance, measuring 0.32 and 0.12 F, respectively. In contrast, in the absence of VO_4^{3-}, these values are lower, at 0.20 and 0.05 F, respectively. These results confirm unequivocally that the addition of VO_4^{3-} inhibits oxidation and improves the capacitive properties of VN in KOH electrolytes.

All-solid-state symmetrical devices are fabricated to evaluate the application potential, in which VN and KOH-VO_4^{3-}/PVA were selected as the electrode and gel electrolyte. As shown in Fig. 5g, the GCD curves of the device

at different current densities are not obviously distorted, illustrating great capacitive characterizations. The specific capacitance is calculated as 296.1 $F{\cdot}cm^{-3}$ (499.5 $F{\cdot}g^{-1}$) at 1 $A{\cdot}cm^{-3}$ (1 $A{\cdot}g^{-1}$) and delivers a high energy density of 40.8 $mWh{\cdot}cm^{-3}$ (69.4 $Wh{\cdot}kg^{-1}$) at 496.7 $mW{\cdot}cm^{-3}$ (843.9 $W{\cdot}kg^{-1}$), which exceeds the majority of previously reported VN-based supercapacitors (Fig. 5h) [35–41]. Additionally, the device is assembled in series to meet the practical needs. The CV curves for single and two-cell configurations in series, acquired at a scan rate of 50 $mV{\cdot}s^{-1}$, are depicted in Fig. S15. The total potential for the two cells in series is 2.0 V, which is exactly twice that of a single device. After full charging, two devices in series could light a commercial green light-emitting diode (LED) bulb with a turn-on voltage of 1.8 V (Fig. 5i). These features demonstrate that the all-solid-state VN symmetrical capacitors are promising devices in energy storage.

4 Conclusion

The capacitance decay mechanism of VN in KOH is investigated comprehensively. The cycling stability of VN decreases sharply in the voltage range of −0.4 to 0 V due to severe oxidation of V–N and N–V–O species in alkaline electrolytes. The specific oxidation process involves interaction of V–N and N–V–O species with dissolved oxygen and O of OH^-. The results reveal that VN oxidation and oxidation product dissolution are responsible for the pseudocapacitance decay and degradation of the electrode materials. Based on the new knowledge of the degradation mechanism, an effective method is demonstrated to enhance the stability and specific capacity of VN electrodes by adding VO_4^{3-} in KOH electrolytes. Our findings contribute to a deeper understanding of the capacity decay of transition metal nitrides in alkaline electrolytes and provide a practical method to improve their electrochemical performance.

Acknowledgements This work was financially supported by the National Natural Science Foundation of China (No. U2004210), Application Foundation Frontier Project of Wuhan Science and Technology Program (No. 2020010601012199), City University of Hong Kong Strategic Research Grant, Hong Kong, China (No. 7005505). The authors are grateful to the facility support provided by the Analytical and Testing Center of WUST.

Declarations

Conflict of interests The authors declare that they have no conflict of interest.

References

[1] Wan LM, Xia QY, Wu JH, Liu J, Shi ZY, Lan S, Zhai T, Savilov SV, Aldoshin SM, Xia H. Stabilizing charge storage of Fe_2O_3-based electrode via phosphate ion functionalization for long cycling life. Rare Met. 2023;42(1):39. https://doi.org/10.1007/s12598-022-02114-x.

[2] Girirajan M, Bojarajan AK, Pulidindi IN, Hui KN, Sangaraju S. An insight into the nanoarchitecture of electrode materials on the performance of supercapacitors. Coord Chem Rev. 2024;518:216080. https://doi.org/10.1016/j.ccr.2024.216080.

[3] He ZH, Gao JF, Kong LB. Electrolyte effect on electrochemical behaviors of manganese fluoride material for aqueous asymmetric and symmetric supercapacitors. Rare Met. 2024;43(3):1048. https://doi.org/10.1007/s12598-023-02515-6.

[4] Chen J, Zhou Y, Huang XY, Yu CY, Han DL, Wang A, Zhu YK, Shi KM, Kang Q, Li PL, Jiang PK, Qian XS, Bao H, Li ST, Wu GN, Zhu XY, Wang Q. Ladderphane copolymers for high-temperature capacitive energy storage. Nature. 2023;615(7950):62. https://doi.org/10.1038/s41586-022-05671-4.

[5] Li H, Chang BS, Kim H, Xie Z, Lainé A, Ma L, Xu T, Yang C, Kwon J, Shelton SW, Klivansky LM, Altoé V, Gao B, Schwartzberg AM, Peng Z, Ritchie RO, Xu T, Salmeron M, Ruiz R, Sharpless KB, Wu P, Liu Y. High-performing polysulfate dielectrics for electrostatic energy storage under harsh conditions. Joule. 2023;7(1):95. https://doi.org/10.1016/j.joule.2022.12.010.

[6] Chettiannan B, Dhandapani E, Arumugam G, Rajendran R, Selvaraj M. Metal-organic frameworks: a comprehensive review on common approaches to enhance the energy storage capacity in supercapacitor. Coord Chem Rev. 2024;518:216048. https://doi.org/10.1016/j.ccr.2024.216048.

[7] Zhang KK, Wang H, Du XB, Dai SG, Wang Y, Liu ML, Cheng SB. Reaction mechanism and structural evolution of tunnel-structured KCu_7S_4 nanowires in Li^+/Na^+-ion batteries. Adv Funct Mater. 2024;34(46):2407105. https://doi.org/10.1002/adfm.202407105.

[8] Xia Q, Xia T, Wu X. PPy decorated α-Fe_2O_3 nanosheets as flexible supercapacitor electrodes. Rare Met. 2022;41(4):1195. https://doi.org/10.1007/s12598-021-01880-4.

[9] Wang XD, Zhou FM, Jing RJ, Gu SY, Zhang Q, Li ZJ, Zhu YJ, Xiao ZZ, Wang L. The precise building units modulation of iron-bismuth sulfide triple-level hierarchical structure for enhanced supercapacitor performance. J Power Sour. 2024;597:234128. https://doi.org/10.1016/j.jpowsour.2024.234128.

[10] Yang YX, Ge KK, Rehman SU, Bi H. Nanocarbon-based electrode materials applied for supercapacitors. Rare Met. 2022;41(12):3957. https://doi.org/10.1007/s12598-022-02091-1.

[11] Kim MJ, Kim M, Sohn WB, Kang J, Kim W, Kang JG. Ultrahigh energy density and ultrafast response in symmetric microsupercapacitors with 3D bicontinuous pseudocapacitance. Adv Energy Mater. 2024;14(42):2402322. https://doi.org/10.1002/aenm.202402322.

[12] Patra D, Pati SK, Muduli S, Mishra S, Park S. Highly planar pseudocapacitive semiconducting polymer electrodes toward symmetric supercapacitors with a wide range of operating potentials. Chem Eng J. 2024;482:149162. https://doi.org/10.1016/j.cej.2024.149162.

[13] Muzaffar A, Ahamed MB, Hussain CM. Green supercapacitors: Latest developments and perspectives in the pursuit of sustainability. Renew Sustain Energy Rev. 2024;195:114324. https://

doi.org/10.1016/j.rser.2024.114324.
[14] Cheng HH, Li JP, Meng T, Shu D. Advances in Mn-based MOFs and their derivatives for high-performance supercapacitor. Small. 2024;20(20):2308804. https://doi.org/10.1002/smll.202308804.
[15] Huang C, Qin P, Li D, Ruan QD, Song H, Liu LL, Wu YZ, Ma YH, Li QW, Huo KF, Chu PK. Origin of superior pseudocapacitive mechanism of transition metal nitrides. J Energy Chem. 2022;69:561. https://doi.org/10.1016/j.jechem.2022.01.041.
[16] Fu YH, Peng YY, Zhao L, He TQ, Yuan MM, Dang H, Liu R, Ran F. Vanadium nitride quantum dots@carbon skeleton anode material synthesized via in situ oxidation initiation strategy. Tungsten. 2024;6(3):561. https://doi.org/10.1007/s42864-023-00246-w.
[17] Zhang YZ, Hu ZW, Li HW, Qiao JQ, Wang XJ, Liu ZM. A conductive flexible carbon nanoyarns embedded with VN quantum dots for highly kinetics-compatible Li-ion capacitors. Chem Eng J. 2024;492:152221. https://doi.org/10.1016/j.cej.2024.152221.
[18] Choi D, Blomgren GE, Kumta PN. Fast and reversible surface redox reaction in nanocrystalline vanadium nitride supercapacitors. Adv Mater. 2006;18(9):1178. https://doi.org/10.1002/adma.200502471.
[19] Gao B, Li XX, Guo XL, Zhang XM, Peng X, Wang L, Fu JJ, Chu PK, Huo KF. Nitrogen-doped carbon encapsulated mesoporous vanadium nitride nanowires as self-supported electrodes for flexible all-solid-state supercapacitors. Adv Mater Interfaces. 2015;2(13):1500211. https://doi.org/10.1002/admi.201500211.
[20] Li QW, Chen Y, Zhang JB, Tian WF, Wang L, Ren ZG, Ren XC, Li XX, Gao B, Peng X, Chu PK, Huo KF. Spatially confined synthesis of vanadium nitride nanodots intercalated carbon nanosheets with ultrahigh volumetric capacitance and long life for flexible supercapacitors. Nano Energy. 2018;51:128. https://doi.org/10.1016/j.nanoen.2018.06.053.
[21] Djire A, Ajenifujah O, Thompson LT. Extent of pseudocapacitance in high-surface area vanadium nitrides. Batter Supercaps. 2018;1(5):1. https://doi.org/10.1002/batt.201800050.
[22] Liu JH, Li FF, Liu WW, Li X. Effect of calcination temperature on the microstructure of vanadium nitride/nitrogen-doped graphene nanocomposites as anode materials in electrochemical capacitors. Inorg Chem Front. 2019;6(1):164. https://doi.org/10.1039/C8QI01071D.
[23] Haye E, Miao YY, Pilloud D, Douard C, Boukherroub R, Pierson JF, Brousse T, Lucas S, Houssiau L, Pireaux JJ. Enhancing cycling stability and specific capacitance of vanadium nitride electrodes by tuning electrolyte composition. J Electrochem Soc. 2022;169(6):063503. https://doi.org/10.1149/1945-7111/ac7353.
[24] Liu Y, Wu QH, Liu LY, Manasa P, Kang L, Ran F. Vanadium nitride for aqueous supercapacitors: a topic review. J Mater Chem A. 2020;8(17):8218. https://doi.org/10.1039/D0TA01490G.
[25] Djire A, Pande P, Deb A, Siegel JB, Ajenifujah OT, He L, Sleightholme AE, Rasmussen PG, Thompson LT. Unveiling the pseudocapacitive charge storage mechanisms of nanostructured vanadium nitrides using in-situ analyses. Nano Energy. 2019;60:72. https://doi.org/10.1016/j.nanoen.2019.03.003.
[26] Zheng K, Xian YQ, Lin ZF. A method for deconvoluting and quantifying the real-time species fluxes and ionic currents using in situ electrochemical quartz crystal microbalance. Adv Mater Interfaces. 2022;9(16):2200112. https://doi.org/10.1002/admi.202200112.
[27] Yang K, Li YW, Jia LL, Wang Y, Wang ZJ, Ji YC, Yang SC, Titirici M, Liu XH, Yang LY, Pan F. Atomic/nano-scale in-situ probing the shuttling effect of redox mediator in Na-O_2 batteries. J Energy Chem. 2021;56:438. https://doi.org/10.1016/j.jechem.2020.08.025.
[28] Wang C, Li XL, Song H, Chu PK, Huo KF. In-plane heterostructured MoN/MoC nanosheets with enhanced interfacial charge transfer for superior pseudocapacitive storage. Adv Funct Mater. 2024;34(12):2311040. https://doi.org/10.1002/adfm.202311040.
[29] Deng DJ, Zhang HH, Wu JC, Zhu LH, Ling M, Dong SH, Li HM, Li HN, Xu L. Co/VN heterojunction anchored on multi-dimensional N-doped carbon for high-performance zinc-air batteries. Mater Today Nano. 2023;24:100409. https://doi.org/10.1016/j.mtnano.2023.100409.
[30] Yang LB, Wang XW, Cheng XM, Zhang YZ, Ma C, Zhang YY, Wang JT, Qiao WM, Ling LC. Regulating Fe aggregation state via unique Fe-N-V pre-coordination to optimize the adsorption-catalysis effect in high-performance lithium-sulfur batteries. Adv Funct Mater. 2023;33(38):2303705. https://doi.org/10.1002/adfm.202303705.
[31] Fang Y, Li L, Gan Y, Gu JJ, Zhang W, Liu JJ, Zhang D, Liu QL. Template-assisted epitaxial growth of ordered SnO_2 nanorods arrays with different hollow structures for high-performance sodium storage. Small. 2024; 2309783. https://doi.org/10.1002/smll.202405322.
[32] Pandey D, Kumar KS, Thomas J. Supercapacitor electrode energetics and mechanism of operation: uncovering the voltage window. Prog Mater Sci. 2024;141:101219. https://doi.org/10.1016/j.pmatsci.2023.101219.
[33] Nègre L, Daffos B, Taberna PL, Simon P. Solvent-free electrolytes for electrical double layer capacitors. J Electrochem Soc. 2015;162(5):A5037. https://doi.org/10.1149/2.0061505jes.
[34] Raj CJ, Manikandan R, Thondaiman P, Sivakumar P, Savariraj AD, Cho WJ, Kim BC, Jung H. Sonoelectrochemical exfoliation of graphene in various electrolytic environments and their structural and electrochemical properties. Carbon. 2021;184:266. https://doi.org/10.1016/j.carbon.2021.08.027.
[35] Lim TS, Ock IW, Lee J, Jo SG, Jung YW, Kwon SH, Song T, Park WI, Lee JW. Freestanding vanadium nitride nanowire/nitrogen-doped graphene paper with hierarchical pore structure for asymmetric supercapacitor anode. J Alloys Compd. 2023;934:167858. https://doi.org/10.1016/j.jallcom.2022.167858.
[36] Liu JH, He X, Guo F, Liu BS, Sun ZJ, Zhang L, Chang HX. Vanadium nitride nanoparticle decorated N-doped carbon nanotube/N-doped carbon nanosheet hybrids via a C_3N_4 self-sacrificing method for electrochemical capacitors. RSC Adv. 2022;12(24):15354. https://doi.org/10.1039/D2RA02789E.
[37] Ramakrishnan K, Surabhi S, Rednam U, Jeong JR, Jeyalakshmi K, Girish S, Morales DV, Viswanathan MR, Karvembu R. Photothermic energy harvesting in reduced graphene oxide nanosheets intercalated with vanadium nitride as pseudocapacitive electrode. ACS Appl Nano Mater. 2024;7:14016. https://doi.org/10.1021/acsanm.4c01118.
[38] Dang H, Wang L, Ran F. Polydopamine supporting method fabricating vanadium nitride nanoparticle enclosed into hierarchical hollow carbon nanospheres for supercapacitors. J Power Sour. 2024;606:234546. https://doi.org/10.1016/j.jpowsour.2024.234546.
[39] Dang H, Wang L, Peng YY, He TQ, Ran F. Hollow nanocages of vanadium nitride-based electrode material designed for superior charging/discharging stability supercapacitors. New J Chem. 2023;47:20377. https://doi.org/10.1039/D3NJ03402J.
[40] Chen MH, Fan H, Zhang Y, Liang XQ, Chen QG, Xia XH. Coupling PEDOT on mesoporous vanadium nitride arrays for advanced flexible all-solid-state supercapacitors. Small. 2020;16(37):2003434. https://doi.org/10.1002/smll.202003434.
[41] Jia HN, Cai YF, Li S, Zheng XH, Miao LF, Wang ZY, Qi JL, Cao J, Feng JC, Fei WD. In situ synthesis of core-shell

vanadium nitride@N-doped carbon microsheet sponges as high-performance anode materials for solid-state supercapacitors. J Colloid Interface Sci. 2020;560:122. https://doi.org/10.1016/j.jcis.2019.10.061.

Springer

RARE METALS

Supporting Information

Capacitance decay mechanism of vanadium nitride supercapacitor electrodes in KOH electrolytes

Xiu-Li Li, Hao Song, Yong-Hui Zhang, Yu-Lei Ren, Qi-Fei Guo, Zi-Huan Tang, Zhuo Li*, Biao Gao*, Paul K. Chu, Kai-Fu Huo*

X.-L. Li, H. Song, Y.-H. Zhang, Y.-L. Ren, Q.-F. Guo, Z.-H. Tang, Z. Li*, B. Gao*
The State Key Laboratory of Refractories and Metallurgy and Institute of Advanced Materials and Nanotechnology, Wuhan University of Science and Technology, Wuhan 430081, China
email: zhuo_li@wust.edu.cn; gaobiao@wust.edu.cn

Paul K. Chu
Department of Physics and Department of Materials Science and Engineering, City University of Hong Kong, Kowloon 999077, Hong Kong, China

K.-F. Huo*
Wuhan National Laboratory for Optoelectronics (WNLO), Huazhong University of Science and Technology, Wuhan 430074, China
email: kfhuo@hust.edu.cn

Xiu-Li Li and Hao Song have contributed equally to this work

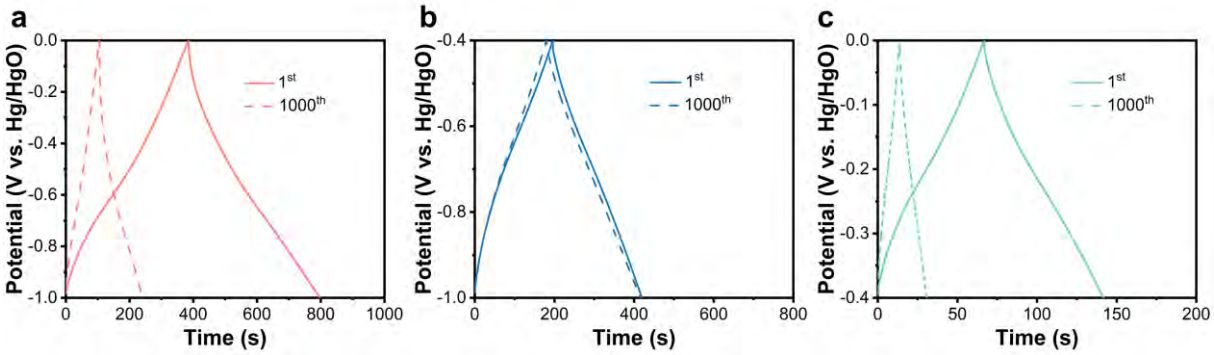

Fig. S1 Galvanostatic charging/discharging (GCD) curves of VN electrode in the 1.0 M KOH electrolyte in the voltage ranges of **a** −1.0 to 0 V, **b** −1.0 to −0.4 V, and **c** −0.4 to 0 V for the first and 1000th cycle at a current density of 1 A·cm^{-3}.

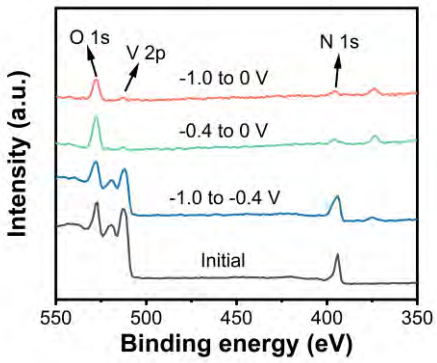

Fig. S2 XPS survey spectra of VN electrode after cycling for different voltage windows.

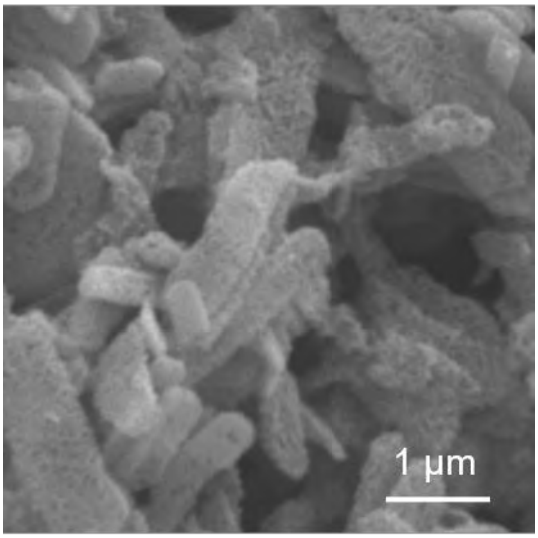

Fig. S3 SEM image of the VN electrode before cycle.

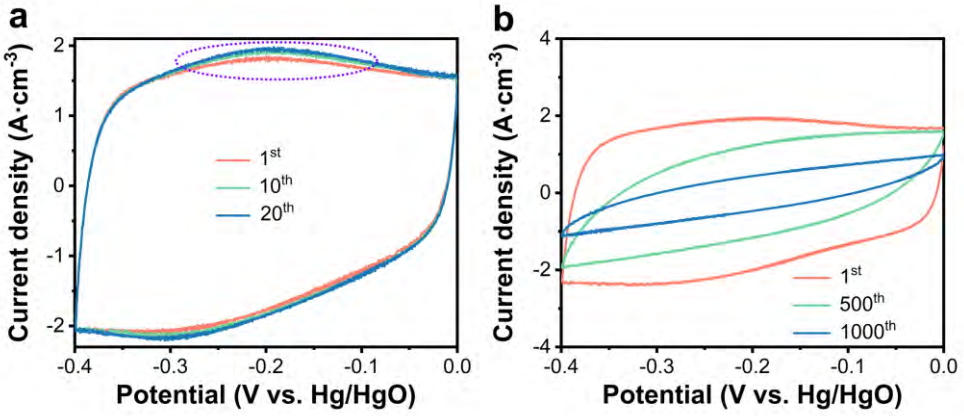

Fig. S4 CV curves of VN electrode for different cycle numbers at a scanning rate of 5 mV·s^{-1} spanning the voltage range of −0.4 to 0 V.

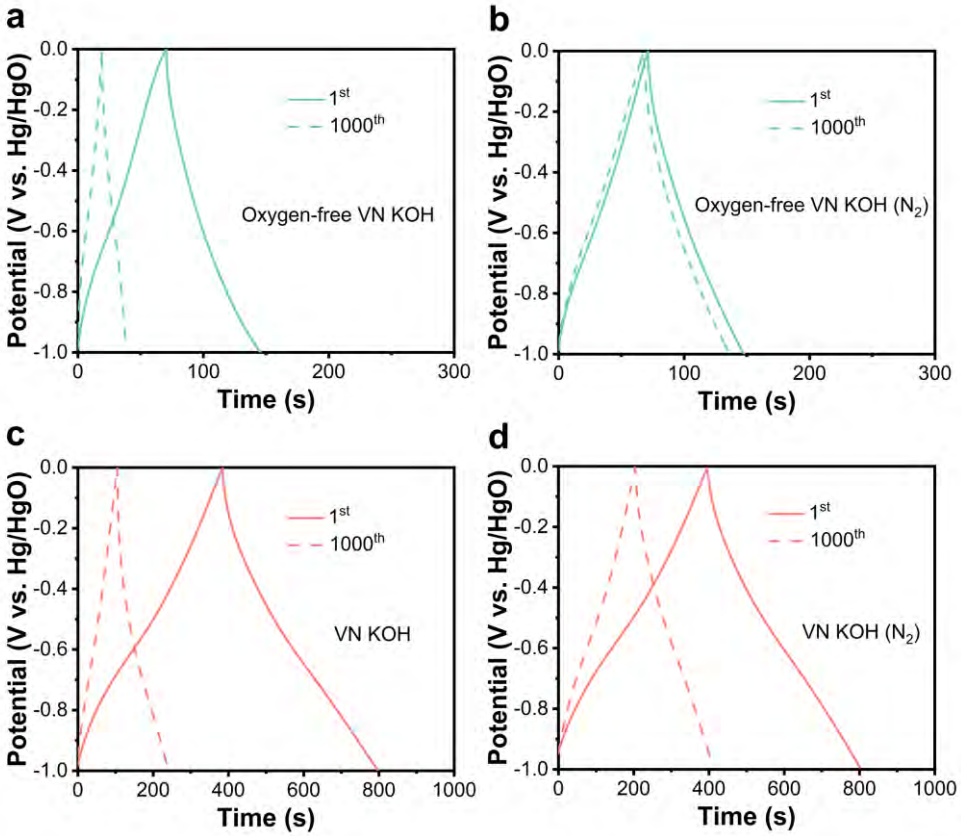

Fig. S5 GCD curves of **a, b** oxygen-free VN and **c, d** VN electrodes without and with bubbling N_2 in 1.0 M KOH for the first and 1000th cycle at a current density of 1 A·cm^{-3}.

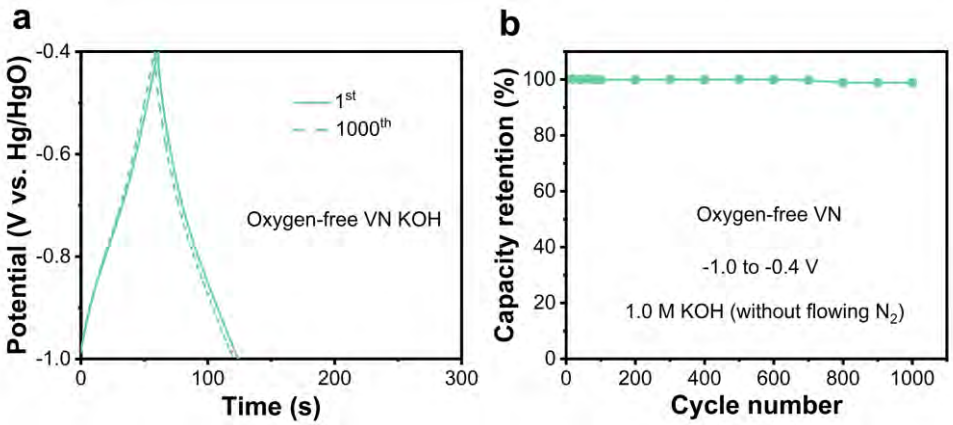

Fig. S6 a GCD curves of the first and 1000th cycle at a current density of 1 A·cm^{-3} and **b** relative capacity retention of oxygen-free VN electrode in the voltage range between −1.0 and −0.4 V.

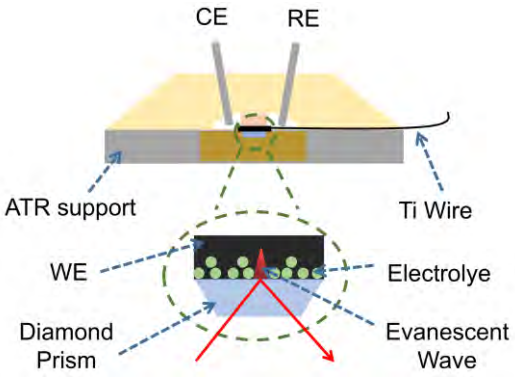

Fig. S7 Schematic diagram of the in situ three-electrode IR cell.

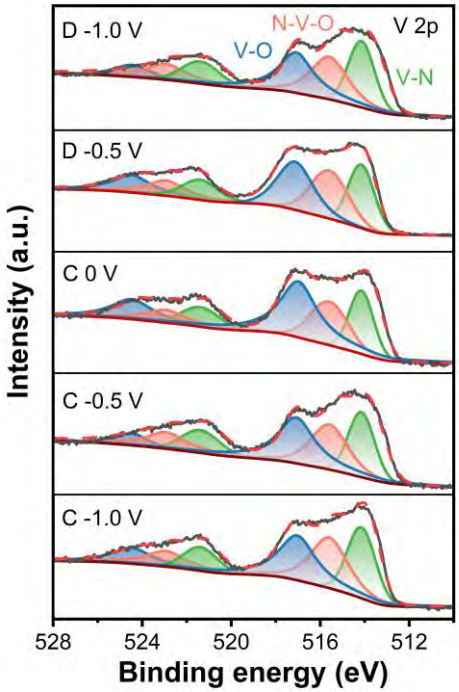

Fig. S8 V 2p spectra of V-O/V-N of VN electrode at different potentials.

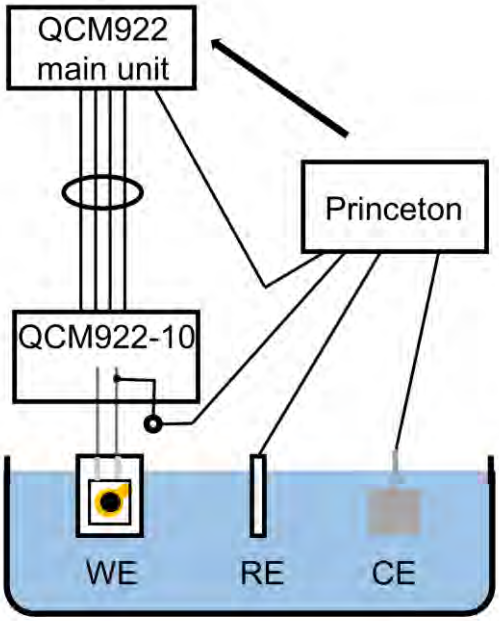

Fig. S9 Schematic diagram of the electrochemical quartz crystal microbalance cell.

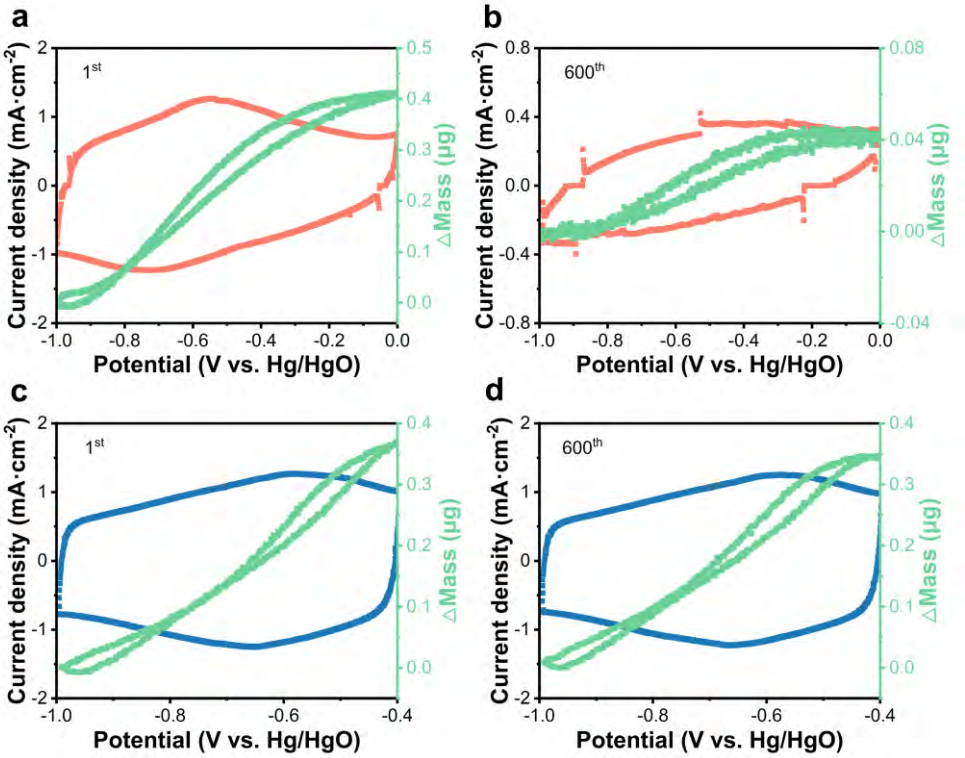

Fig. S10 CV curves (20 mV·s^{-1}) and mass change of VN-coated quartz electrode during cycling in the voltage ranges of **a, b** −1.0 to 0 V and **c, d** −1.0 to −0.4 V.

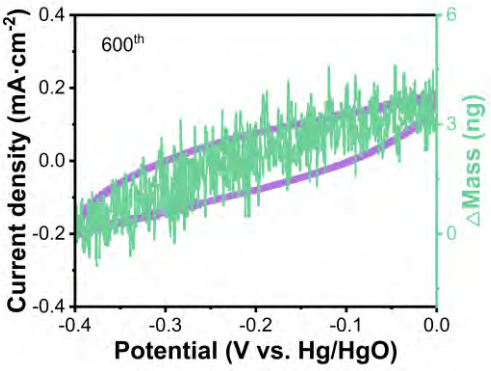

Fig. S11 600th cycle CV curve (20 mV·s^{-1}) and mass change of the VN-coated quartz electrode in the voltage ranges of −0.4 to 0 V.

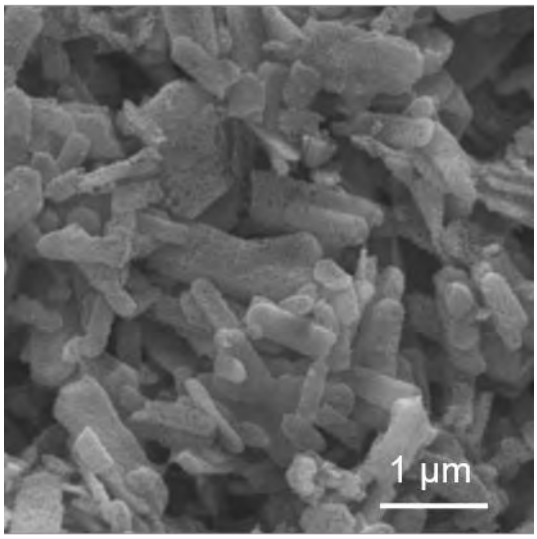

Fig. S12 SEM image of VN electrode after cycling in the 1.0 M KOH electrolyte with the addition of 0.2 M VO_4^{3-}.

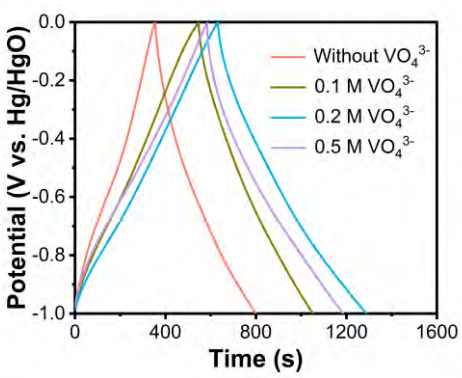

Fig. S13 GCD curves of VN electrode in the 1.0 M KOH electrolyte addition different content of VO_4^{3-} at a current density of 1 $A \cdot cm^{-3}$.

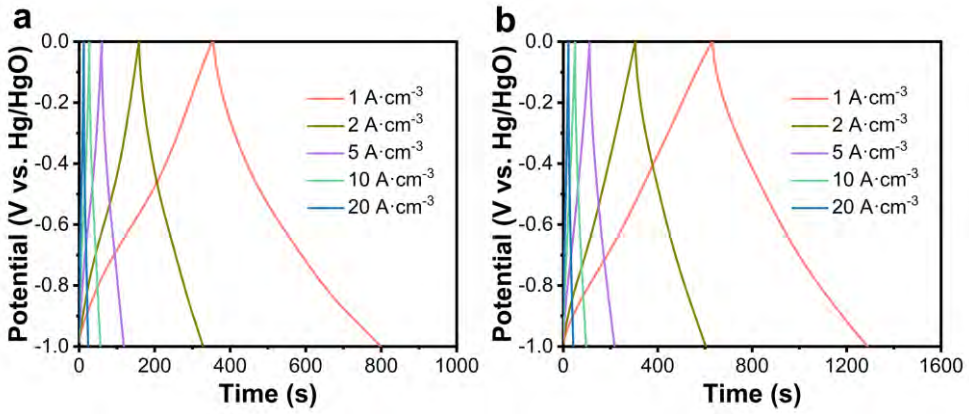

Fig. S14 GCD curves of VN electrode at the different current densities in the 1.0 M KOH electrolyte **a** without and **b** with the addition of 0.2 M VO_4^{3-}.

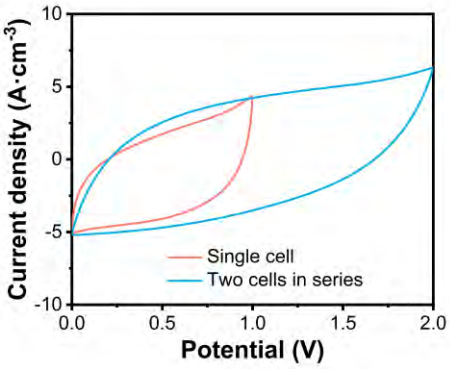

Fig. S15 The CV curves of single and two cells in series acquired at 50 mV·s^{-1}.

Table S1 Fitting parameters for V 2p spectra taken from VN electrode to calculate the contents of V-N and V-O at different potentials.

Potential	V 2p species	Peak area	V-O/V-N ratio
C −1.0 V	V-O	14103	1.20
	V-N	11753	
C −0.5 V	V-O	10470	1.48
	V-N	7061	
C 0 V	V-O	14361	1.87
	V-N	7680	
D −0.5 V	V-O	21607	1.52
	V-N	14216	
D −1.0 V	V-O	8312	1.32
	V-N	6297	